Research Square

Preprints are preliminary reports that have not undergone peer review.
They should not be considered conclusive, used to inform clinical practice,
or referenced by the media as validated information.

Deep-learning instance segmentation and explainable rule-based classification to resolve platelets, red blood cells and aggregates in imaging flow cytometry

Andreas Gerhard Wild
Stellenbosch University
Chantelle Venter
chantellev@sun.ac.za
Stellenbosch University
Willem Jacobus Perold
Stellenbosch University
Thomas Niesler
Stellenbosch University
Etheresia Pretorius
Stellenbosch University

Article

Keywords: Platelets, Inflammation, Long COVID, Imaging Flow Cytometry, Deep Learning, Instance Segmentation

Posted Date: November 16th, 2026

DOI: https://doi.org/10.21203/rs.3.rs-11287429/v1

License: This work is licensed under a Creative Commons Attribution 4.0 International License.
Read Full License

Additional Declarations: Competing interest reported. A.G. Wild has a commercial interest in the segmentation technology described in this work. E. Pretorius and W.J. Perold are founding directors of BioCode Technologies. C. Venter and T.R. Niesler declare no competing interests.

Deep-learning instance segmentation and explainable rule-based classification to resolve platelets, red blood cells and aggregates in imaging flow cytometry

A.G. Wild[1†], C. Venter[2*†], W.J. Perold[3], T.R. Niesler[3], E. Pretorius[2,4]

[1]Institute for Biomedical Engineering, Stellenbosch University, Stellenbosch, South Africa.
[2]Department of Physiological Sciences, Stellenbosch University, Stellenbosch, South Africa.
[3]Department of Electrical and Electronic Engineering, Stellenbosch University, Stellenbosch, South Africa.
[4]Department of Biochemistry, Cell and Systems Biology, Institute of Systems, Molecular and Integrative Biology, Faculty of Health and Life Sciences, University of Liverpool, Liverpool, United Kingdom.

*Corresponding author(s). E-mail(s): chantellev@sun.ac.za;
Contributing authors: 24991104@sun.ac.za; wjperold@sun.ac.za;
trn@sun.ac.za; resiap@sun.ac.za;
†These authors are co-first authors.

Abstract

Platelets link blood clotting with inflammation and are studied in conditions such as Long COVID. With imaging flow cytometry (IFC) the small, low-contrast and touching objects of the platelet fraction remain difficult to segment and classify, which motivates a deep-learning approach. This study presents a pipeline that pairs a fine-tuned Cellpose3 instance segmentation model with an explainable rule-based decision tree. On held-out images, the segmentation model achieved a mean average precision (mAP) of 0.665, compared to 0.143 for a classical threshold method. Each object is classified as a platelet, red blood cell (RBC) or aggregate. On 3000 hand-labeled images, the classification agreed with human annotation on 83.4% of objects. Four blood sample preparation methods were compared, including a high-yield platelet optimization (HPO) method. A pilot cohort of eleven control and nine Long COVID participants was analyzed. Platelet, RBC and aggregate concentrations in the HPO fraction were higher in the Long COVID cohort. These differences are not clearly due to underlying biology and the results are hypothesis-generating.

Keywords: Platelets, Inflammation, Long COVID, Imaging Flow Cytometry, Deep Learning, Instance Segmentation

Introduction

Platelets are classically defined by their central role in hemostasis and thrombosis [1] and are increasingly recognized as more than just cells relevant for bleeding arrest [2, 3]. Activated platelets also provide a surface that supports the coagulation cascade. Platelet activation assists in wound healing, and plays an important role in tissue remodeling after injury to the endothelial barrier and to the subendothelial tissue. Platelet activation may also result in pathological clot formation that may contribute to pathologies seen in inflammatory diseases. Additionally, Factor XII of the intrinsic pathway is involved in platelet activation with the coagulation cascade during immune reactions [4, 5]. Upon activation, platelets release various molecules that are stored inside their δ-granules, α-granules, and lysosomes [6]. These stored molecules interact directly with leukocytes, other platelets, erythrocytes and the endothelium [7, 8]. The released molecules can include pathogenic amyloid β peptides [9].

Importantly, platelets are incorporated into the fibrin clot during clot formation [10]. Fibrin is actively formed on the surface of activated platelets [11], thus supporting thrombus growth and thrombin capture. Molecules stored in their granules also interact with fibrin(ogen) during platelet activation. Ultimately, platelet activation is at the intersection of coagulation, immune pathologies and inflammation. It has been suggested that platelets are the predominant immune cells in circulation involved in chronic inflammation, responses to infections, and autoimmune disorders [5].

The platelet fraction of blood provides a view into the pathologies associated with thrombo-inflammatory conditions. Studying platelets, however, is notoriously difficult. They are extremely sensitive to their environment and become activated in response to even minor mechanical, chemical, or thermal perturbation. As a result, much of the

signal recorded in a platelet assay can be introduced by the assay itself. The choice of anticoagulant, the speed and duration of centrifugation, storage temperature, and the delay between draw and analysis have all been shown to alter the measured activation state [12–14].

An additional challenge is the isolation and definition of the platelet fraction itself. Several preparation methods are commonly used, e.g. whole blood (WB) or platelet-rich plasma (PRP). Each method trades purity, yield, and the risk of *ex vivo* activation. WB assays minimize handling, but they leave platelets among red blood cells (RBCs), which outnumber them by more than an order of magnitude. PRP enriches platelets at the cost of centrifugation steps that may themselves activate the cells [15]. Additionally, residual RBCs could be misclassified as platelets on the basis of size alone.

Flow cytometry is the established reference method for characterizing platelet activation [16, 17]. Markers such as PAC-1, which recognizes the activated conformation of the GPIIb/IIIa (integrin αIIbβ3) fibrinogen receptor, are used [18]. Additionally, CD62P (P-selectin), which is externalized upon α-granule release, is employed [19]. The conventional CD235a marker is chosen for RBCs. Conventional flow cytometry, however, records only integrated fluorescence and light-scatter per event and discards spatial information. This makes it hard to separate a single platelet from a platelet–platelet aggregate, a platelet–RBC aggregate, or from debris of comparable scatter. Imaging flow cytometry (IFC) addresses this gap by capturing a brightfield image and multiple fluorescence images of every event. This technique combines the throughput of traditional flow cytometry with the morphological analysis power of microscopy [20–22]. This is especially valuable for the platelet fraction, where size, shape, and aggregation state carry as much information as marker intensity. The bottleneck therefore shifts from data acquisition to data analysis. Thousands of small, low-contrast, frequently touching objects must be segmented reliably before per-cell morphological features can be computed. Classical thresholding copes poorly with overlapping cells and aggregates. This suggests that modern deep-learning segmentation approaches that can delineate individual objects even when they are clustered together might be useful [23, 24]. Deep learning has previously been applied to IFC images for cell classification [25, 26]. Image-based classification of platelet aggregates by agonist type has also been demonstrated [27]. Nishikawa *et al.* [28] used massive image-based profiling to show high levels of circulating platelet aggregates in patients with COVID-19.

Interest in the platelet fraction has been renewed by reports of platelet hyperactivation and a pro-thrombotic phenotype in acute SARS-CoV-2 infection [29–35]. The same phenomenon persists in post-acute sequelae of SARS-CoV-2, commonly termed Long COVID [36–41]. Measuring the extent to which platelet concentration, activation, and interaction with RBCs differ in this population requires a robust method. Such a method should be reproducible despite the pre-analytical challenges discussed above and be capable of resolving platelets, RBCs, and aggregates in the same sample.

This paper presents an IFC analysis pipeline. Deep-learning-based instance segmentation and a rule-based decision tree classify each event as a platelet, RBC or aggregate. Four sample preparation methods are compared. These include a novel

method intended to recover platelets and aggregates entrapped in the hematocrit. The pipeline is then applied to an exploratory comparison of a control and a Long COVID cohort. Two questions are addressed. The first is whether the new method separates platelet marker signal from RBCs better than the other RBC-containing methods. The second is whether platelet, RBC and aggregate populations differ between the two cohorts. Population concentration, PAC-1 and CD62P fluorescence are compared between cohorts.

Results

Each IFC event was segmented with a fine-tuned Cellpose3 model. Each mask was then classified as a platelet, RBC or aggregate by a hand-crafted decision tree. Full details are given in the Methods. The validation of the pipeline is presented first. The four sample preparation methods are then compared. Finally, the control and Long COVID cohorts are compared. Fluorescence microscopy results are presented in the supplementary material, as validation for IFC results and a final comparison between the control and Long COVID cohorts.

Pipeline Validation

The fine-tuned segmentation model was evaluated on the 2016 held-out images, which contain 3644 annotated objects. The model achieved a mean average precision (mAP) of 0.665. The average precision at an intersection over union threshold of 0.5 was 0.866. The classical baseline achieved a mAP of 0.143 and an average precision of 0.402 at the same 0.5 threshold. The held-out images were used in the stopping criterion during training, so the values of the fine-tuned model are slightly optimistic and are validation rather than test performance.

The classification pipeline was compared with Annotator 1 on the 3000 image validation set. Annotator 1 labeled 40 images as background noise that do not contain a valid event. These images are misclassifications of the pipeline, since the noise filter did not remove them. These 40 images were excluded, so the scores below are computed over 2960 images. The proposed classification pipeline achieved an 84.5% agreement and a Cohen's κ of 0.77 with Annotator 1. The 95% confidence interval of the agreement is 83.1% to 85.8%. When the 40 noise images are counted as errors, the agreement over all 3000 images is 83.4%. Furthermore, the classification pipeline achieved macro-averaged precision, recall and F1 values of 0.84, 0.86 and 0.84, respectively. These scores are computed on a sample balanced over the predicted classes and are not weighted by the prevalence of each class.

All five human annotators assigned the same class to 36 of the 50 images. Among the human annotators, a Fleiss' κ of 0.811 was obtained. The mean pairwise agreement between human annotators was 87.4%, with a mean Cohen's κ of 0.811. Individual pairs of annotators agreed on between 80.0% and 94.0% of images, with Cohen's κ values between 0.70 and 0.91. In comparison, the classification pipeline achieved a mean pairwise agreement of 91.2% and a mean Cohen's κ of 0.868 with the five human annotators. When the classification pipeline is included as a sixth rater, Fleiss' κ increased from 0.811 to 0.830. Scored against the consensus label, the classification

pipeline achieved a 96.0% agreement and a Cohen's κ of 0.940, with per-class F1 values of 0.97, 0.94 and 0.97 for the platelet, RBC and aggregate classes, respectively. The 95% confidence interval of this agreement is 86.5% to 98.9%. The agreement of the classification pipeline with the human annotators was within the range of agreement between the annotators.

Sample Preparation

The high-yield platelet optimization (HPO) method was designed to recover and enhance the yield of platelets, platelet aggregates and platelet–RBC aggregates that are entrapped in the hematocrit. This analysis asks whether it does so better than the other fractions that contain RBCs, namely the hematocrit and WB. Two measures are used. The first is the ratio between platelet and RBC median fluorescence, which measures how well platelet-marker signal separates from the RBC internal negative control. The second is the number of platelet and aggregate events per RBC event, which measures how strongly a method enriches the populations of interest relative to RBCs. Being a within-sample ratio, it is unaffected by the different dilutions of each method. Table 1 reports both measures, together with the median platelet fluorescence, as the median and interquartile range over all participants ($n = 20$).

Table 1: **Sample preparation comparison.** Each donor ($n = 20$) contributes one value per method; entries are the median [IQR] across donors. Platelet intensity is the median platelet fluorescence (a.u.). Platelet/RBC fluorescence is the ratio of platelet to RBC median fluorescence; a ratio near 1 indicates platelet signal indistinguishable from the RBC negative control. Events per RBC is the number of platelet or aggregate events per RBC event in the same sample.

	HPO	Hematocrit	WB	PRP
Platelet intensity (a.u.)				
PAC-1	84 [53–176]	29 [28–29]	29 [29–29]	51 [45–54]
CD62P	178 [138–245]	27 [26–27]	27 [27–27]	98 [94–115]
Platelet/RBC fluorescence				
PAC-1	1.73 [1.12–3.92]	1.00 [1.00–1.00]	1.04 [1.00–1.04]	n/a†
CD62P	1.95 [1.28–2.71]	1.00 [1.00–1.00]	1.00 [1.00–1.02]	n/a†
Events per RBC				
Platelets	0.126 [0.100–0.233]	0.044 [0.038–0.054]	0.051 [0.045–0.066]	n/a†
Aggregates	0.264 [0.210–0.509]	0.192 [0.181–0.202]	0.218 [0.201–0.271]	n/a†

†Undefined, since PRP is depleted of RBCs by design.

PRP is excluded from this ranking by design. Centrifugation removes the RBCs and pellets the larger aggregates, so a PRP sample cannot contain all three populations of the primary endpoint. The median area of aggregates in PRP is 46 µm^2,

compared to 111 µm^2 to 185 µm^2 in the other methods. Furthermore, the events classified as RBCs in PRP have a median area of 34 µm^2, roughly half that of the RBCs in the other methods (≈64 µm^2). These events are therefore mostly misclassified platelets rather than true RBCs. Consequently, both RBC-referenced measures in Table 1 are undefined for PRP. Nonetheless, the platelets in PRP were stained with median intensities of 51 and 98 in arbitrary units (a.u.) for PAC-1 and CD62P, respectively. These are above the background level of the hematocrit and WB methods, but below that of the HPO method.

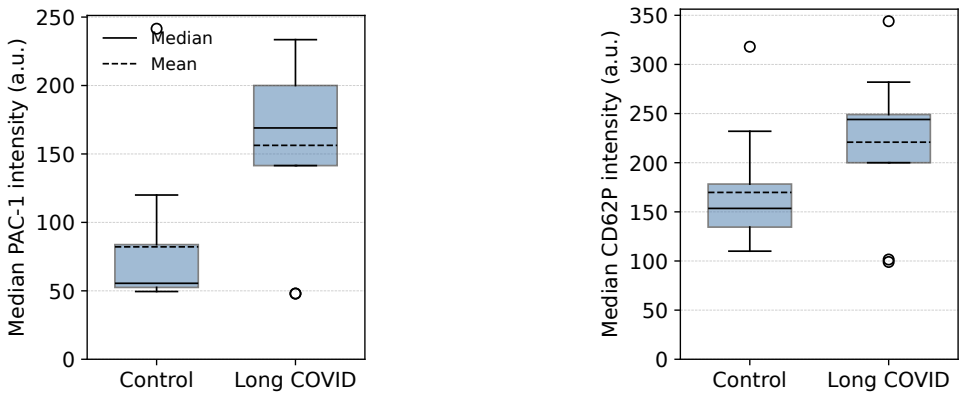
Among the RBC-containing methods, HPO performed best on both measures. The platelet/RBC fluorescence ratios were 1.73 and 1.95 for PAC-1 and CD62P, respectively, whereas the hematocrit and WB ratios were close to 1. Platelet PAC-1 and CD62P intensities were higher in HPO than in the hematocrit and WB methods. In these two methods the platelet, aggregate and RBC intensities all lie at the same background level of approximately 28 a.u., which indicates that platelet staining was too weak to separate platelets from the RBC background in IFC. Furthermore, HPO yielded 0.126 platelet events per RBC event, compared to 0.044 and 0.051 for the hematocrit and WB methods. This is a two- to three-fold enrichment of platelets relative to RBCs. The enrichment of aggregates was smaller, with 0.264 aggregate events per RBC event for HPO, compared to 0.192 and 0.218 for the hematocrit and WB methods. These results are consistent with the choice of HPO as the preparation method for the primary endpoint. The following subsections focus on data collected with the HPO method.

Platelet Activation Markers

Platelet activation between the control and Long COVID cohorts was investigated. Figure 1 reports the median PAC-1 and CD62P intensity. These measurements are in arbitrary units since the fluorescence intensity is dependent on equipment calibration. Notably, calibration settings were kept constant during the data acquisition steps in this study to ensure uniformity between samples.

Median PAC-1 and CD62P intensities of the platelet population were higher in the Long COVID cohort. These differences were not larger than those of the RBC noise floor. Table 2 displays the results of the Mann–Whitney U test performed on this data. The Benjamini–Hochberg adjusted p-value, p_{BH}, and Cliff's δ resulting from the Mann–Whitney U test are reported.

The platelet population produced Cliff's δ values between 0.23 and 0.41, which correspond to small to medium effect sizes according to Romano *et al.* [42]. The corresponding p_{BH} values were between 0.297 and 0.483, so these estimates are uncertain. The aggregate and RBC populations produced mixed results with no consistent trend. Since RBCs express neither marker, the RBC population acts as a noise floor for this comparison. Its Cliff's δ values are of similar magnitude to those of the platelet population, so the platelet trend cannot be distinguished from noise at this sample size. The aggregate population contains platelets, but also RBC-only aggregates, which may dilute any platelet signal.



a PAC-1 **b** CD62P

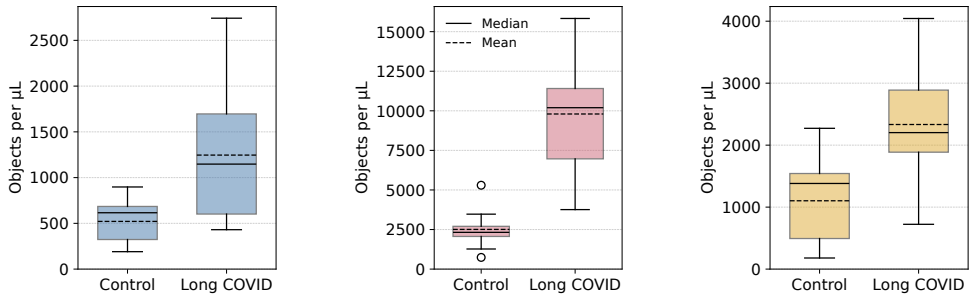
Fig. 1: **Median platelet fluorescence intensity of the control and Long COVID cohorts in the HPO fraction.** Fluorescence intensity is associated with platelet activation. Boxes show the interquartile range, with the median as a solid line and the mean as a dashed line. Whiskers extend to the furthest participant within 1.5 times the interquartile range. Points beyond the whiskers are individual outliers.

Table 2: **Comparison of platelet activation markers between the control and Long COVID cohorts in the HPO fraction.** Values are medians over donors of the per-donor statistic. P95 is the 95$^{\text{th}}$ percentile. A positive Cliff's δ indicates higher values in the Long COVID cohort.

Population	Marker	Statistic	Control	Long COVID	Cliff's δ	p_{BH}
Platelet	PAC-1	Median	55.5	169	0.41	0.297
		P95	324	601	0.27	0.431
	CD62P	Median	154	244	0.39	0.297
		P95	534	772	0.23	0.483
Aggregate	PAC-1	Median	46.5	43.0	−0.62	0.237
		P95	52.5	56.1	0.31	0.381
	CD62P	Median	85.8	87.0	−0.13	0.707
		P95	110	122	0.47	0.297
RBC	PAC-1	Median	47.0	44.0	−0.56	0.237
		P95	62.0	247	0.33	0.381
	CD62P	Median	89.0	89.5	−0.04	0.909
		P95	216	379	0.43	0.297

Population Concentrations

The primary endpoint is to determine whether the concentrations of platelets, RBCs and aggregates differ between the control and Long COVID cohorts. The HPO method



a Platelets **b** RBCs **c** Aggregates

Fig. 2: **IFC concentrations of each cell population in the HPO fraction of the control and Long COVID cohorts.** An upward trend in cell concentration is observed between the control and Long COVID cohort. Boxes show the interquartile range, with the median as a solid line and the mean as a dashed line. Whiskers extend to the furthest participant within 1.5 times the interquartile range. Points beyond the whiskers are individual outliers.

was selected *a priori* for this endpoint, and the results of the sample preparation comparison showed that it was the most successful of the RBC-containing preparation methods. For this reason, this subsection focuses on the HPO method.

Table 3 displays the Benjamini–Hochberg corrected p and Cliff's δ values for the Mann–Whitney U test between the control and Long COVID cohort for the HPO sample preparation method.

Table 3: **Median population concentration, in objects per µL, compared between the control and Long COVID cohorts in the HPO fraction.** The p-value, Benjamini–Hochberg corrected across the three populations, is presented as p_{BH}. Values are medians over donors of the per-donor concentration.

Population	Control	Long COVID	Cliff's δ	p_{BH}
Platelet	616	1147	0.64	0.019
RBC	2321	10 196	0.98	$<$0.001
Aggregate	1382	2202	0.72	0.012

Concentrations were higher in the Long COVID cohort for all three populations. Cliff's δ was 0.64, 0.98 and 0.72 for the platelet, RBC and aggregate populations, respectively. All three effects are large according to Romano *et al.* [42]. The corresponding p_{BH} values were 0.019, < 0.001 and 0.012. Figure 2 displays box and whisker plots for the objects per µL for each population between each cohort.

The full results of the Mann–Whitney U tests are reported in Supplementary Table S5. The absolute count exploratory endpoint closely mimicked the results presented in Table 3. This is expected, since all HPO samples were acquired with near-identical volumes (≈13 µL). The absolute count is a direct proxy for concentration and not an independent endpoint.

Large differences were also observed in the exploratory comparison of the PRP method. Platelet and aggregate concentrations were higher in the Long COVID cohort, with Cliff's δ of 0.70 and 0.68, respectively. The corresponding p_{BH} values were 0.039 and 0.036. The RBC result for PRP in Supplementary Table S5 should not be interpreted, since RBCs are removed by design.

For the HPO method, all three concentrations were higher in the Long COVID cohort, with large effect sizes. Note that these are concentrations in the prepared HPO fraction rather than in whole blood. The proportion of platelets and aggregates among all objects was lower in the Long COVID cohort, which may be attributed to a higher RBC yield. Cliff's δ was -0.45 and -0.52, with p_{BH} values of 0.126 and 0.077, respectively. The Long COVID HPO fraction was more cellular rather than enriched in platelets. The RBC concentrations of the hematocrit and WB fractions were similar between cohorts, with Cliff's δ of -0.03 and -0.01, as seen in Supplementary Table S5. The large RBC difference in the HPO fraction, with $\delta = 0.98$, is therefore unlikely to reflect RBC counts in whole blood.

Discussion

This study used four different sample preparation techniques with fluorescence microscopy and IFC. A new deep-learning-based pipeline was used for IFC analysis. In the HPO fraction, platelet, RBC and aggregate concentrations were higher in the Long COVID cohort than in the control cohort, with large effect sizes. The largest difference was in RBCs, and the Long COVID fraction contained fewer platelets per RBC. Platelet PAC-1 and CD62P intensities showed small to medium effects that could not be distinguished from noise. Previous studies have reported circulating activated platelets in Long COVID [36, 37, 40]. The present data can neither confirm nor refute these reports. High levels of circulating platelet aggregates have also been reported in acute COVID-19 [28]. Earlier IFC work reported platelet–monocyte aggregates in Long COVID [21]. However, the cohort comparison of this study is exploratory. Platelet hyperactivation could not be confirmed at the sample size of this study.

Among the RBC-containing methods, HPO gave the clearest platelet-marker separation and the greatest platelet enrichment. Platelet fluorescence intensity in the WB and hematocrit methods was too weak to separate platelets from the RBC background in IFC. The added FBS, HetaSep and incubation at 36 °C of the HPO method may also activate platelets *ex vivo*. Platelets are sensitive to such handling steps [12, 14]. This effect is considered unlikely to explain the cohort difference. In the HPO micrographs of Supplementary Fig. S10, control platelets showed minimal activation. Long COVID platelets prepared in the same way showed pseudopodia and spreading. A similar cohort difference was reported in a centrifuged cellular fraction [43]. In that study, platelet inhibitors did not change platelet activation during processing. The

HPO method may still interact with biochemical changes in Long COVID blood. Long COVID platelets may be more sensitive to the handling steps than control platelets. This possibility is hypothesis-generating and requires further study.

Platelets with pseudopodia and spreading were visible in fluorescence micrographs, provided in Supplementary Figs. S8 to S11, of the PRP, hematocrit, HPO and WB methods. Microscopy is a qualitative method that views individual platelets at higher magnification, and may not require as large an intensity difference to reveal activated morphology such as pseudopodia and platelet spreading. Qualitatively, more activated morphology was seen in the Long COVID HPO and hematocrit micrographs. This is in line with previous research [43]. No such difference was seen in the PRP micrographs. In the WB micrographs, activated platelets and clumping were seen in both cohorts. Further research is required to explain why the WB micrographs differ from the IFC results.

The HPO concentrations may depend on the efficiency of HetaSep sedimentation. This efficiency was not measured between cohorts. Therefore, the cohort differences in the HPO fraction may partly reflect the separation step rather than blood composition. The aggregate population is defined by touching masks and was not subdivided into RBC–RBC, platelet–RBC and platelet–platelet aggregates. Since the RBC concentration was higher in the Long COVID HPO fraction, part of the aggregate increase may consist of RBC-only aggregates or coincident events. In a coincident event, unrelated cells are imaged in the same frame and appear connected. However, the proportion of aggregates was lower in the more concentrated Long COVID samples. Coincidence is therefore unlikely to dominate. Its contribution was not quantified. Platelet differences were not confined to the HPO fraction. The PRP fraction showed large platelet effects in the exploratory comparison.

This study has limitations. The cohort is small, with eleven control and nine Long COVID participants. No *a priori* power analysis was performed, and only large effects of approximately Cliff's $\delta \geq 0.68$ were detectable with 80% power, hence the activation comparison was underpowered. Small samples also tend to inflate estimated effect sizes [44]. The large δ values of the concentration comparison should be read with caution. The null result of the activation comparison should be read as inconclusive rather than negative. The sex ratio differed between the cohorts and was not adjusted for. Full blood counts were not recorded and the HPO concentrations cannot be normalized to the blood composition of each participant. Platelet counts are partly coupled to the activation markers, but switching the marker rule off changed the HPO platelet counts by less than 0.5%.

The classification pipeline was validated on the HPO method and the performance on the other methods is unknown, although images from different sample preparation methods are indistinguishable. Annotator 1 designed the classification rules and labeled the 3000 image set, which may favour agreement with the pipeline. The 50 image set was labeled independently by four further annotators. The decision tree rules also have known failure modes, whose effects were minimised where possible. Round platelet masks with a major axis between 7 px and 8 px may be classified as RBC-like. Fully side-on RBCs are assigned to the irregular population. The fluorescence microscopy is qualitative, unblinded and based on representative images.

A fine-tuned Cellpose3 segmentation model combined with an explainable rule-based decision tree can classify platelets, RBCs and aggregates in IFC brightfield images. A total of 29.6 million masks were segmented over all 20 participants. The agreement of the pipeline with human annotators was within the range of agreement between the annotators themselves. The pipeline is therefore suitable, as validated on the HPO fraction, for the object-level analysis of platelet fractions that contain RBCs and aggregates.

Of the RBC-containing preparation methods, the HPO method gave the clearest separation of platelet marker signal from the RBC background. The HPO method is therefore recommended when platelets and aggregates entrapped in the hematocrit are of interest.

A platelet activation difference between the cohorts could not be confirmed. Platelet, RBC and aggregate concentrations in the HPO fraction were higher in the Long COVID cohort. The largest difference was in RBCs, which the separation step is designed to remove. The concentration differences may therefore reflect separation efficiency of the preparation method rather than blood composition. The cohort comparison is therefore hypothesis-generating.

Future work should report the input and output cell counts of the HPO method, so that concentrations can be normalized to recovery. A larger cohort with full blood counts is required. Aggregates should be classified into sub-populations, and the contribution of coincident events should be quantified. The analysis code and per-object features are openly available to support future work.

Methods

This section begins with a brief description of the collected samples and ethical clearance. Then, the physical blood collection procedure is discussed with respect to the four preparation methods used in this study. Additional sample preparation and staining steps are discussed, followed by the procedure used for fluorescence microscopy analysis. Finally, the IFC and data analysis procedures are provided. Here, data analysis includes a discussion of the deep-learning-based segmentation model, the rule-based decision tree to isolate populations of interest and the statistical methods applied to these cell populations to quantify the differences between cohorts.

Demographics and Ethical Clearance

Long COVID was diagnosed by a qualified medical practitioner. This diagnosis required patients to present novel and persistent symptoms subsequent to the acute phase of COVID-19 infection [45]. The control cohort ($n = 11$) comprised four males and seven females and had a mean age of 37.9 ± 14.8 years. Similarly, the Long COVID cohort ($n = 9$) had five male and four female participants, with a mean age of 41.6 ± 14.9 years. Ages are given as mean $\pm$ s.d. Comorbidities present in the Long COVID participants are listed in Supplementary Table S1.

Ethical clearance was granted by the Health Research Ethics Committee of Stellenbosch University, South Africa. This study (project ID: 31384) made use of anonymous samples collected under the Stellenbosch University Blood Laboratory Biorepository

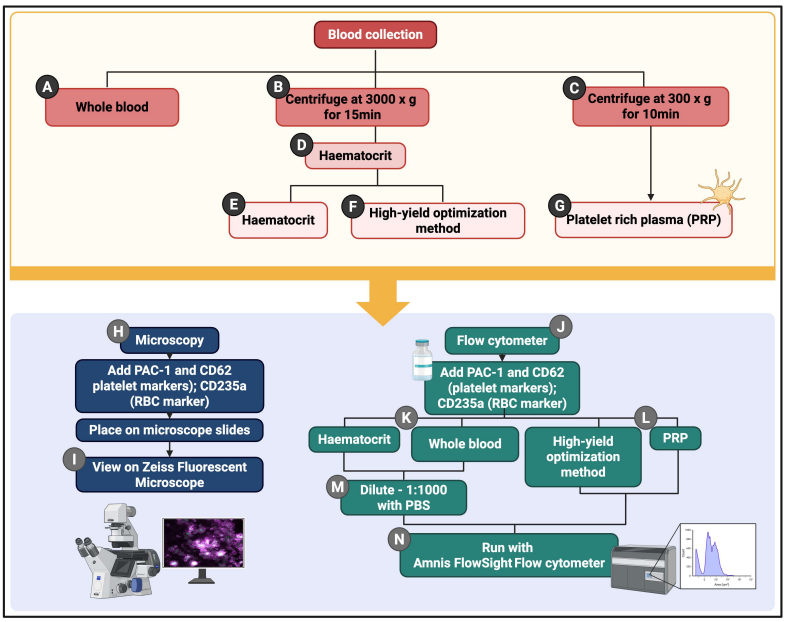


Fig. 3: **Preparation methods used for fluorescence microscopy and IFC.** For the different preparation methods, one tube was used for WB (A), and the remaining blood in that tube was centrifuged at 300 × g (C) for 10 minutes for the PRP (G) fraction. A second tube was centrifuged at 3000 × g (B) for 15 minutes for the hematocrit fraction (D). From the hematocrit fraction, the standard hematocrit method (E) was performed, as well as the new HPO method (F). Each fraction was stained once with PAC-1, CD62P and, except for PRP, CD235a. The samples were then prepared for either the microscope (H), by placement on microscope slides and viewing with the Zeiss fluorescence microscope (I), or for IFC (J). To run the samples on the IFC, the hematocrit and WB fractions (K) were diluted 1:1000 in phosphate-buffered saline (M), whereas the HPO and PRP fractions (L) were not diluted further, before acquisition on the Amnis FlowSight (N). Created with BioRender.com.

(project ID: 28804). All Biorepository samples were obtained with voluntary informed consent, including consent for storage and future use in approved studies. All research protocols were conducted in accordance with the Declaration of Helsinki, the South African Guidelines for Good Clinical Practice, and the Ethical Guidelines for Research issued by the South African Medical Research Council.

Blood Collection Procedure

Two citrate blood tubes were drawn by a qualified phlebotomist or medical practitioner from consenting volunteers of the control and Long COVID cohort. Figure 3 illustrates the four preparation methods after blood collection, as well as the sample preparation steps for both IFC and fluorescence microscopy. Samples were collected between February and April 2024.

After collection, one tube was used for the WB analysis (Fig. 3A). The blood needed for the WB analysis was aliquoted. Thereafter, the remaining blood was centrifuged at $300 \times g$ for 10 minutes to obtain the PRP (Fig. 3C).

The other collected tube was centrifuged for 15 minutes at $3000 \times g$ at room temperature to obtain the required hematocrit fractions (Fig. 3B). This hematocrit fraction was used for both the standard hematocrit preparation method and the HPO method (Fig. 3D). The two hematocrit methods are discussed below. All laboratory methods were completed within 12 hours of blood sample collection.

Fluorescence Staining for Platelet Visualization

This subsection gives the sample preparation steps before the application of IFC or fluorescence microscopy. These steps cover the fluorescence staining and incubation procedure for each of the four preparation methods. Antibody volumes followed the recommendations of the manufacturers.

Platelet-Rich Plasma

After the PRP centrifugation step, 60 µL of the PRP was placed in a 1.5 mL tube. Then, 12 µL CD62P (PE-conjugated, clone CLB-Thromb/6, IM1759U, Beckman Coulter, Brea, CA, USA, RRID:AB_3755077) and 12 µL PAC-1 (FITC-conjugated, clone PAC-1, 340507, BD Biosciences, San Jose, CA, USA, RRID:AB_2230769) were added. Finally, the solution was incubated at room temperature for 30 minutes and was protected from light. CD235a was not added to the PRP fraction, as it does not contain RBCs. The PRP fraction was analyzed using IFC and fluorescence microscopy as described below.

Whole Blood and Hematocrit

The method used for WB and hematocrit was identical, bar centrifugation, and is discussed here. After centrifugation, the plasma was removed from the hematocrit fraction. Next, 4 µL CD62P (PE-conjugated), 4 µL PAC-1 (FITC-conjugated) and 1 µL CD235a (Brilliant Violet 421-conjugated, clone HI264, 349132, BioLegend, San Diego, CA, USA; supplied by Biocom Africa, South Africa, RRID:AB_2941527) was added to 20 µL of both the WB and the hematocrit. The samples were incubated at room temperature for 30 minutes, while being protected from light.

After incubation, the WB and hematocrit samples were diluted 1:1000 in phosphate-buffered saline (Fig. 3M). The diluted blood was analyzed with IFC, while the undiluted blood was used for fluorescence microscopy as described below.

High-Yield Platelet Optimization Fraction

Here, the HPO method seen in Fig. 3F is discussed. The method is intended to recover platelets, platelet aggregates and platelet–RBC aggregates entrapped in the hematocrit. The new method was performed by adding 50 µL of the hematocrit to 50 µL of complete media (RPMI+20% FBS) and 100 µL of HetaSep (STEMCELL Technologies, CAT#07806) in a dilution ratio of 1:1:2. HetaSep is conventionally used to

separate nucleated cells from RBCs. Here, HetaSep is applied to recover the platelet fraction retained in the hematocrit. After gentle mixing, 140 µL of the 1:1:2 sample was placed in a 500 µL tube, with the lid closed and incubated at 36 °C for 5 minutes to allow separation.

Separation resulted in two fractions: an HPO fraction (Fig. 3F) and a hematocrit-derived RBC fraction. Then, 40 µL of the HPO fraction was placed in a 1.5 mL tube, followed by the addition of 8 µL each of the fluorescence platelet markers CD62P (PE-conjugated) and PAC-1 (FITC-conjugated), and 2 µL CD235a. The fraction was incubated for a further 30 minutes at room temperature, while being protected from light. After incubation, the HPO fraction was analyzed by IFC and fluorescence microscopy (Fig. 3H and J).

Fluorescence Microscopy

After incubation, 10 µL of each of the four fractions was placed on a microscope slide. This analysis was done to corroborate the IFC results. The samples were then viewed with a Zeiss Axio Observer 7 fluorescence microscope, seen in Fig. 3I, with a Plan-Apochromat 63×/1.4 Oil DIC M27 objective (Carl Zeiss Microscopy, Munich, Germany). The excitation wavelength for PAC-1 was set at 450 nm to 488 nm and the emission at 499 nm to 529 nm. The CD62P excitation was set at 540 nm to 570 nm, with emission at 577 nm to 607 nm. Finally, the CD235a excitation was set at 370 nm to 400 nm and the emission from 410 nm to 440 nm.

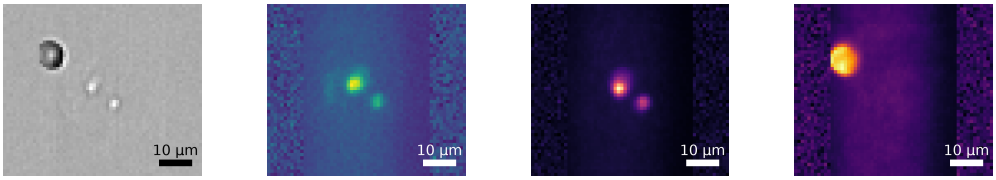
Imaging Flow Cytometry

This study was conducted with IFC as main imaging modality and quantification method. Images were acquired on an Amnis FlowSight imaging flow cytometer using INSPIRE software (version 200.0.336.0; Cytek Biosciences, Fremont, CA, USA). Images were acquired with the 20× objective of the FlowSight, which gives a nominal pixel size of 1×1 µm. The raw IFC files are extracted and all further processing was completed in Python 3.14. Cell masks were created with a deep-learning segmentation model instead of the threshold masks of the instrument software.

Each collected blood sample was processed using four different methods: PRP, hematocrit, WB and HPO. The primary endpoint of the study is to investigate whether cell concentrations differ between the control and Long COVID populations. Three cell populations are targeted in this study: platelets, RBCs and aggregates. Here, aggregates are denoted as two or more cells that are connected. The HPO method was selected *a priori* as the preparation method for the primary endpoint. The method was developed to recover the platelet populations targeted in this study. A secondary analysis compares HPO with the other RBC-containing methods, hematocrit and WB. Optimality of preparation method is measured by the separation between platelet and RBC fluorescence, and by the enrichment of platelets and aggregates relative to RBCs. PRP is excluded from this comparison, since it is RBC-depleted by design and cannot contain all three target populations.

Figure 4 contains typical examples of events imaged with IFC. All the samples were stained with the PAC-1, CD62P and CD235a fluorescence markers. PAC-1 and

CD62P were excited at 488 nm, and CD235a was excited at 405 nm. The PAC-1 and CD62P markers are both closely associated with platelet activation, while CD235a is a well-known RBC membrane marker.



a Brightfield **b** PAC-1 **c** CD62P **d** CD235a

Fig. 4: Examples of the fluorescence emission of different markers in IFC, with a 10 µm scale bar.

One RBC and two platelets are present in Fig. 4a. Internally a fourth irregular population is defined, in addition to platelet, RBC and aggregate, to be everything not targeted by the study. This avoids aberrant events being forced into membership with the target populations.

Brightfield images were recorded in channels 1 and 9. Images from channel 1 were used in this work. PAC-1 was recorded in channel 2, with a 528/65 nm emission filter. CD62P was recorded in channel 3, with a 577/35 nm filter. CD235a was recorded in channel 7, with a 457/45 nm filter. Side scatter was recorded in channel 6. All channels were recorded with 12-bit time delay integration charge-coupled device cameras. The laser powers were 80 mW at 405 nm and 60 mW at 488 nm. Side scatter was excited at 785 nm with a power of 3.59 mW. Samples were acquired at the medium flow speed setting, and acquisition was stopped after a set sample volume had been acquired. The built-in calibration of the instrument, ASSIST, was run with calibration beads every morning before sample processing. A median of 294 148 events was acquired per HPO sample, with a range of 194 989 to 453 379. The acquired volume of every HPO sample was between 12.98 µL and 13.29 µL.

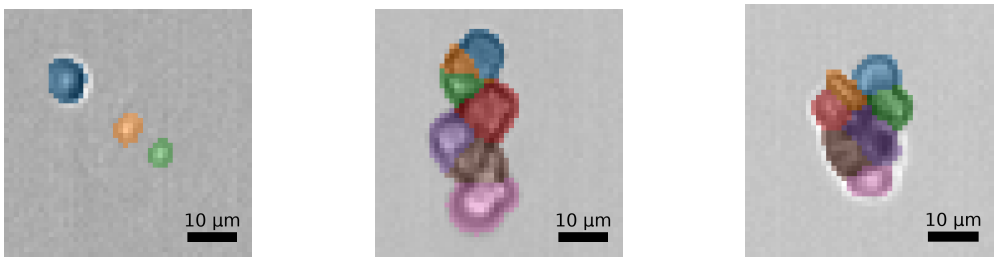
Brightfield and fluorescence images are extracted from the raw IFC files. Spectral crosstalk was corrected with the compensation matrix stored in each raw file. The crosstalk matrix was set in the INSPIRE software before the study and is presented in Supplementary Fig. S1. Linear unmixing was applied per pixel as $c = S^{-1}m$, with the vector of measured intensities across all acquired channels m, compensation matrix S and compensated intensities c.

Data Analysis

The analysis is described in five parts. These are segmentation, feature extraction, population classification, pipeline validation and statistical analysis.

Segmentation

Image segmentation is the process of creating masks or overlays for objects of interest in images. In this study the objects of interest are the cells in the brightfield images returned from IFC. Instance segmentation with a single class is used to mask the cells. Two further methods of segmentation exist, namely semantic and panoptic [46], although they are not discussed in the interest of brevity. An advantage of instance segmentation is that two cells in the same image are seen as distinct entities. Overlapping or connected cells are expected in the context of platelet activation, which is investigated in this study.



a **b** **c**

Fig. 5: Examples of instance segmentation in IFC, with a 10 µm scale bar.

Traditionally, images from IFC are not masked using instance segmentation. Figure 5 illustrates the usefulness of this type of segmentation. For example, the masks in Fig. 5b may be used to classify the cells as an aggregate. Without this type of segmentation it would be difficult to discern a single large cell from many small cells clumped together.

The conventional analysis workflow for Amnis instruments is the IDEAS software, which combines threshold-based masks with manual gating. IDEAS produces semantic masks, which assign pixels to an object class but do not separate touching objects into instances. A direct comparison with IDEAS was therefore not possible at the level of individual objects. Instance segmentation of IFC brightfield images is not yet established. No instance-level gold standard exists for comparison. Instead, the segmentation is compared with a classical threshold and watershed baseline. The complete classification pipeline is also validated against human annotators.

Segmentation is achieved by using a pre-trained convolutional neural network (CNN) that has been fine-tuned on IFC data. The Cellpose3 model introduced by Stringer and Pachitariu in 2025 [47] is chosen because it is a mature and generalist model, which can be fine-tuned on modest hardware [48, 49]. This model has been fine-tuned on an unpublished dataset of approximately 10 000 IFC images, which was annotated by the authors for the purpose of training an instance segmentation model. It is composed of IFC acquisitions that are independent of the samples used for this study. No pre-processing or post-processing was applied to the brightfield input images. A single pass through the model results in the masks shown in Fig. 5.

Cellpose3 is based on the U-net architecture [50]. For fine-tuning, the IFC image dataset was split into 8076 training and 2016 held-out images. The checkpoint with the lowest loss on the held-out images was retained. The architecture and training details are provided in Supplementary Note 1.

The mAP is calculated to evaluate the accuracy of the model. The average precision is calculated at different intersection over union thresholds that range from 0.5 to 0.95 in steps of 0.05. This method follows the standard set by the COCO image segmentation challenge [51]. The held-out images were segmented with the same inference settings as the study samples. Here, the study samples are the brightfield images of every IFC acquisition in this study. The default inference settings of Cellpose 3.0.9 were used, and are listed in Supplementary Table S2. A classical baseline approach to instance segmentation was evaluated on the same held-out images. This baseline applies a Yen threshold [52], followed by a distance transform and watershed [53] to separate touching objects. The fine-tuned model was used for cell segmentation of all samples collected during this study. Segmentation of the samples used Cellpose 3.0.9 and PyTorch 2.11 [54]. The dataset of approximately 10 000 images was only used to train and test the segmentation model and was not used for the classification of platelets, RBCs and aggregates in this work.

Feature Extraction

Provided that high quality masks are available, features that describe the spatial, geometric and textural characteristics of the cell can be easily calculated. Supplementary Table S3 shows all the features calculated for all the segmented cells. Most of the features are calculated using the `scikit-image` Python library [55], version 0.26.0, with the exception of the `distance_to_edge`, `connected_to` and intensity features. These features are implemented from scratch. The features may be used to gate the imaged cells into various populations. For example, platelets have a diameter of roughly 2–3 µm [56], whereas RBCs have a diameter of about 8 µm [57]. This difference enables the separation of cells into two populations, based on their `equivalent_diameter` feature.

Population Classification

The analysis task in this study is to classify every cell into one of three classes: platelet, RBC or aggregate. Should a cell be unfit for membership to any one of these classes, it is classified as the irregular population. Many of the images captured during the IFC process are empty images with no visible event. Most of these images were disregarded by the segmentation model and no masks were calculated. However, in some cases the model attempts to segment the noisy background, which produces erroneous masks. The first step in data analysis is to remove these incorrect masks. Masks with `bf_std_intensity` < 8 are removed. A value of 8 is chosen based on the empirical histogram provided in Supplementary Fig. S2. Once the obviously incorrect masks have been removed, the population classification commences. Here, classification refers to a hand-crafted deterministic decision tree, seen in Supplementary Fig. S3, and should not be confused with the classical machine learning algorithm of the same name. The

approach followed in this study is related to rule-based gating strategies typically employed in IFC studies.

First, all masks are given a shape attribute, which describes the population the mask likely belongs to. These per-mask shape attributes are resolved into per-object populations once touching masks have been grouped. A mask is `RBC-like` when it has the correct size *or* fluorescence signal *and* has the correct shape. A mask has the correct size or fluorescence signal when one of the following is true:

- `major_axis` ≥ 7 px *or*
- `equivalent_diameter` ≥ 8 px *or*
- median fluorescence signal `CD235a` ≥ 1000.

Masks are the correct shape when they are compact and round according to the following rule:

- `solidity` ≥ 0.88 *and*
- `eccentricity` ≤ 0.85.

Masks that satisfy both rules receive the `RBC-like` shape attribute. The threshold values are chosen based on the underlying biology of the cells of interest and the instrumentation used in the study.

The size thresholds were set between the mask sizes of the two cell types. Median platelet masks have an equivalent diameter of about 5 px. Median RBC masks have an equivalent diameter of about 9 px. Brightfield masks are larger than the cells at this pixel size. The `major_axis` and CD235a rules recover RBCs that are tilted relative to the camera. CD235a positivity is not required for the `RBC-like` attribute. Only 10% of the `RBC-like` masks in HPO reached the CD235a threshold, and none did in the hematocrit and WB methods. CD235a was not added to the PRP fraction, so the CD235a rule is inactive for PRP. The reasoning behind each threshold is provided in Supplementary Note 2.

Masks that fail the membership test of RBCs are tested again. A mask is `platelet-like` when it is small on both size measurements and CD235a-negative, and is either round or carries a true platelet activation signal. True platelet activation, PAC-1 or CD62P fluorescence positivity, is defined per sample preparation method against an internal negative control. RBCs express neither PAC-1 nor CD62P. As such the 99^{th} percentile of each marker among the `RBC-like` masks of that method, pooled over all participants of both cohorts, provides a threshold value. A mask is called PAC-1 or CD62P positive if the median intensity is above this threshold. Note that this threshold is only meaningful in RBC-containing fractions. In PRP the `RBC-like` masks are mostly misclassified platelets, so the PRP threshold is inflated. Any remaining mask that is neither `RBC-like` nor `platelet-like` is assigned the shape `other`.

At this point all masks have been assigned a shape attribute of `platelet-like`, `RBC-like` or `other`. Since all masks are instance level segmentations, the connected instances may be calculated. Any two or more masks that have at most one pixel separating them are connected and grouped together to become a single entity. These grouped cells form the population group aggregate. All the remaining single cell masks inherit their population from their shape attribute. This procedure is followed for all

masks returned by the segmentation model. Representative events of each population are shown in Supplementary Fig. S4, Supplementary Fig. S5 and Supplementary Fig. S6.

Pipeline Validation

The exploratory analyses depend on the populations calculated from this classification pipeline. Therefore, the classification logic is validated on a subset of 3000 hand-labeled images. Here, labeling involves assigning a class of platelet, RBC or aggregate to an event when provided with a brightfield image. This allows the end-to-end accuracy of the entire pipeline to be estimated relative to human performance. The validation set is sampled from the HPO preparation method, over both cohorts and equally weighted over all classes predicted by the pipeline. The 3000 image validation set was labeled by the first author, referred to as Annotator 1. Annotator 1 also designed the classification rules. The pipeline class was hidden during labeling.

The sampling was stratified by the class predicted by the pipeline. Per-class precision is therefore estimated directly. However, the overall agreement is not weighted by class prevalence. Events assigned to the irregular population were not sampled. Events removed by the noise filter or missed by segmentation are also not assessed.

To estimate inter-annotator variability, a second validation set of 50 images was labeled independently by four more human annotators. Again, images were sampled from both cohorts of the HPO preparation method and stratified according to the class assigned by the classification pipeline. Each annotator was presented with the unprocessed brightfield image of every event. The annotators assigned one of the three classes, platelet, RBC or aggregate, to the central object of each image. Annotators were blinded to the output of the classification pipeline and did not have contact with each other. The 50 images and their labels are shown in Supplementary Fig. S7 and Supplementary Table S4.

Agreement between each pair of raters, where the classification pipeline is treated as an additional rater, is reported as the percentage agreement and Cohen's κ [58]. Agreement among all raters is summarized using Fleiss' κ [59] computed over the images. Pairwise scores are computed in a similar fashion. Furthermore, a consensus label is assigned to every image by majority vote of the five human annotators. The classification pipeline is then scored against this consensus label using percentage agreement, Cohen's κ and per-class precision, recall and F1.

Statistical Analysis

The primary endpoint is cell concentration, compared between the control and Long COVID cohorts. Three exploratory endpoints are also reported: absolute cell count, % of total, and median cell area. Each endpoint is compared with an unpaired, two-sided Mann–Whitney U test [60]. Since the participant is the unit of analysis, tested quantities are the median value of cell features per participant. The treatment of individual cells as independent observations would result in pseudoreplication [61]. The test is unpaired because the control ($n = 11$) and Long COVID ($n = 9$) cohorts comprise different individuals and two-sided because no direction of effect is specified. At these sample sizes normality cannot be assumed, motivating the rank-based test.

Two quantities are reported per endpoint. The first is the p-value. For the primary endpoint, the p-values of the HPO method are Benjamini–Hochberg [62] corrected across the three populations. All other comparisons are exploratory and are reported descriptively. Their p-values are Benjamini–Hochberg corrected across the four endpoints within each preparation method and population. The second is Cliff's δ [63], interpreted using the thresholds of Romano *et al.* [42]: $|\delta| < 0.147$ negligible, $0.147 \leq |\delta| < 0.33$ small, $0.33 \leq |\delta| < 0.474$ medium, and $|\delta| \geq 0.474$ large. Cliff's δ is treated as the primary measure of the size of each difference. The p-value is reported as an exact value and serves as a measure of statistical uncertainty. Values of p below 0.001 are reported as < 0.001.

The sample size was set by the number of available participants. No *a priori* power analysis was performed. A simulation of the Mann–Whitney U test at the present group sizes gives 80% power at $\alpha = 0.05$ only for effects of approximately Cliff's $\delta \geq 0.68$. The simulation drew 4000 samples per effect size from two normal distributions that differ in location.

A secondary analysis compares the platelet marker staining of the three RBC-containing preparation methods. The participant remains the unit of analysis. Every participant is measured under all four methods. Two measures estimate which RBC-containing method is optimal. First, the ratio between the median fluorescence intensity of the platelet and RBC populations is calculated per participant. This quantity measures how well the platelet-marker signal separates from the RBC internal negative control. The larger the ratio the easier the separation. Second, the number of platelet and aggregate events per RBC event is calculated per participant. This measures the enrichment of the populations of interest relative to RBCs. As a within-sample ratio, it is unaffected by the different dilutions of each method. Both measures use RBCs as reference and are therefore not reported for PRP.

Finally, an investigation into platelet activation was conducted between the control and Long COVID cohort. For each mask, the median fluorescence intensity is calculated and then averaged over the masks of each object. Then, for each participant, the median and 95^{th} percentile over all the objects in each population are calculated. These per-participant values are used as the test endpoints. Again an unpaired, two-sided Mann–Whitney U test is conducted to measure the difference between the two cohorts. In addition to the Benjamini–Hochberg corrected p-values, the Cliff's δ values are also reported. The Benjamini–Hochberg correction was applied across all 12 activation comparisons of the HPO method.

All statistics are completed in Python 3.14 with version 1.18.0 of the `scipy.stats` module [64]. The analysis code and the data required to reproduce the results are available as described in the data availability statement.

An AI language model was used to assist with editing the text and reasoning. The authors take responsibility for all text.

Acknowledgements. Model fine-tuning was performed on Rhasatsha, the HPC1 cluster of Stellenbosch University, http://www.sun.ac.za/hpc. Figure 3 was created with BioRender.com under a publication license held by E. Pretorius.

Funding. No specific grant was received for this work. Laboratory costs were covered by the research funds of E. Pretorius, Department of Physiological Sciences, Stellenbosch University.

Author contributions. A.G.W., C.V. and E.P. conceptualised the study and developed the methodology. A.G.W. developed the software, curated the data, performed the formal analysis and validated the pipeline. C.V. performed the experiments and administered the project. E.P. acquired the funding, administered the project and supervised the work. W.J.P. and T.R.N. supervised the work. A.G.W. and C.V. prepared the figures. A.G.W., C.V. and E.P. wrote the manuscript. A.G.W., C.V., E.P. and T.R.N. reviewed and edited the manuscript. All authors approved the final manuscript. The roles of each author according to the CRediT taxonomy are listed in Supplementary Table S6.

Data availability. The image features of all 29.6 million segmented masks are archived on Zenodo, with DOI 10.5281/zenodo.22895198. The features are provided as parquet files and are released under a CC BY 4.0 license. The shared data are de-identified and carry cohort labels only. Open deposit of these data was approved by the Health Research Ethics Committee of Stellenbosch University. The consent obtained covers the sharing of de-identified, participant-level data. The raw IFC files are available from the corresponding author on reasonable request.

Code availability. The analysis code is maintained on GitHub at https://github.com/Andreas-Wild/platelet-hyperactivation. A versioned release will be archived on Zenodo on acceptance. The fine-tuned segmentation model is deposited on Zenodo with restricted access, with DOI 10.5281/zenodo.22895731. Access is restricted because the model is subject to a commercial interest of an author. Access is granted on request for non-commercial research under the PolyForm Strict License 1.0.0. Access is conditional on agreeing not to use the model or its outputs to build datasets or to train other models. The training dataset is not publicly available.

Competing interests. A.G. Wild has a commercial interest in the segmentation technology described in this work. E. Pretorius and W.J. Perold are founding directors of Biocode Technologies. C. Venter and T.R. Niesler declare no competing interests.

References

[1] Larsen, J. B., Hvas, A.-M. & Hojbjerg, J. A. Platelet function testing: update and future directions. *Seminars in Thrombosis and Hemostasis* **49**, 600–608 (2023).

[2] Mack, A., Vanden Hoek, T. & Du, X. Thromboinflammation and the role of platelets. *Arteriosclerosis, Thrombosis, and Vascular Biology* **44**, 1175–1180 (2024).

[3] Koupenova, M., Clancy, L., Corkrey, H. A. & Freedman, J. E. Circulating platelets as mediators of immunity, inflammation, and thrombosis. *Circulation Research* **122**, 337–351 (2018).

[4] Mezger, M. *et al.* Platelets and immune responses during thromboinflammation. *Frontiers in Immunology* **10**, 1731 (2019).

[5] Kumari, P., Panigrahi, A. R., Yadav, P., Beura, S. K. & Singh, S. K. Platelets and inter-cellular communication in immune responses: dialogue with both professional and non-professional immune cells. *Advances in Protein Chemistry and Structural Biology* **140**, 347–379 (2024).

[6] Chen, Y., Yuan, Y. & Li, W. Sorting machineries: how platelet-dense granules differ from α-granules. *Bioscience Reports* **38**, BSR20180458 (2018).

[7] Weisel, J. W. & Litvinov, R. I. Red blood cells: the forgotten player in hemostasis and thrombosis. *Journal of Thrombosis and Haemostasis* **17**, 271–282 (2019).

[8] Grobler, C. *et al.* Covid-19: the rollercoaster of fibrin(ogen), D-dimer, von Willebrand factor, P-selectin and their interactions with endothelial cells, platelets and erythrocytes. *International Journal of Molecular Sciences* **21**, 5168 (2020).

[9] Wolska, N. *et al.* Human platelets release amyloid peptides β1–40 and β1–42 in response to hemostatic, immune, and hypoxic stimuli. *Research and Practice in Thrombosis and Haemostasis* **7**, 100154 (2023).

[10] Höök, P. *et al.* Strong binding of platelet integrin αIIbβ3 to fibrin clots: potential target to destabilize thrombi. *Scientific Reports* **7**, 13001 (2017).

[11] Swieringa, F., Spronk, H. M., Heemskerk, J. W. & van der Meijden, P. E. Integrating platelet and coagulation activation in fibrin clot formation. *Research and Practice in Thrombosis and Haemostasis* **2**, 450–460 (2018).

[12] Hindle, M. S., Cheah, L. T., Yates, D. M. & Naseem, K. M. Preanalytical conditions for multiparameter platelet flow cytometry. *Research and Practice in Thrombosis and Haemostasis* **7**, 102205 (2023).

[13] Jourdi, G. *et al.* Consensus report on flow cytometry for platelet function testing in thrombocytopenic patients: communication from the SSC of the ISTH. *Journal of Thrombosis and Haemostasis* **21**, 2941–2952 (2023).

[14] Cattaneo, M. *et al.* Recommendations for the standardization of light transmission aggregometry: a consensus of the working party from the platelet physiology subcommittee of SSC/ISTH. *Journal of Thrombosis and Haemostasis* **11**, 1183–1189 (2013).

[15] Perez, A. G. *et al.* Relevant aspects of centrifugation step in the preparation of platelet-rich plasma. *International Scholarly Research Notices* **2014**, 176060 (2014).

[16] Michelson, A. D. Flow cytometry: a clinical test of platelet function. *Blood* **87**, 4925–4936 (1996).

[17] Frelinger, A. L. *et al.* Consensus recommendations on flow cytometry for the assessment of inherited and acquired disorders of platelet number and function: communication from the ISTH SSC Subcommittee on Platelet Physiology. *Journal of Thrombosis and Haemostasis* **19**, 3193–3202 (2021).

[18] Shattil, S. J., Cunningham, M. & Hoxie, J. A. Detection of activated platelets in whole blood using activation-dependent monoclonal antibodies and flow cytometry. *Blood* **70**, 307–315 (1987).

[19] Stenberg, P. E., McEver, R. P., Shuman, M. A., Jacques, Y. V. & Bainton, D. F. A platelet alpha-granule membrane protein (GMP-140) is expressed on the plasma membrane after activation. *Journal of Cell Biology* **101**, 880–886 (1985).

[20] Hui, H., Fuller, K. A., Erber, W. N. & Linden, M. D. Imaging flow cytometry in the assessment of leukocyte-platelet aggregates. *Methods* **112**, 46–54 (2017).

[21] Thompson, A. *et al.* An imaging flow cytometry method to study platelet-monocyte aggregates using Long COVID as a model. *bioRxiv* (2026). Preprint.

[22] Rees, P., Summers, H. D., Filby, A., Carpenter, A. E. & Doan, M. Imaging flow cytometry. *Nature Reviews Methods Primers* **2**, 86 (2022).

[23] Moen, E. *et al.* Deep learning for cellular image analysis. *Nature Methods* **16**, 1233–1246 (2019).

[24] Caicedo, J. C. *et al.* Evaluation of deep learning strategies for nucleus segmentation in fluorescence images. *Cytometry Part A* **95**, 952–965 (2019).

[25] Eulenberg, P. *et al.* Reconstructing cell cycle and disease progression using deep learning. *Nature Communications* **8**, 463 (2017).

[26] Lippeveld, M. *et al.* Classification of human white blood cells using machine learning for stain-free imaging flow cytometry. *Cytometry Part A* **97**, 308–319 (2020).

[27] Zhou, Y. *et al.* Intelligent classification of platelet aggregates by agonist type. *eLife* **9**, e52938 (2020).

[28] Nishikawa, M. *et al.* Massive image-based single-cell profiling reveals high levels of circulating platelet aggregates in patients with COVID-19. *Nature Communications* **12**, 7135 (2021).

[29] Rohlfing, A.-K., Rath, D., Geisler, T. & Gawaz, M. Platelets and COVID-19. *Hämostaseologie* **41**, 379–385 (2021).

[30] Barale, C., Melchionda, E., Morotti, A. & Russo, I. Prothrombotic phenotype in COVID-19: focus on platelets. *International Journal of Molecular Sciences* **22**, 13638 (2021).

[31] Barrett, T. J. *et al.* Platelets amplify endotheliopathy in COVID-19. *Science Advances* **7**, eabh2434 (2021).

[32] Subramaniam, S., Reinhardt, C., Kulkarni, P. P. & Spiezia, L. COVID-19 and thrombo-inflammatory responses. *Frontiers in Cardiovascular Medicine* **10**, 1231909 (2023).

[33] Manne, B. K. *et al.* Platelet gene expression and function in patients with COVID-19. *Blood* **136**, 1317–1329 (2020).

[34] Hottz, E. D. *et al.* Platelet activation and platelet-monocyte aggregate formation trigger tissue factor expression in patients with severe COVID-19. *Blood* **136**, 1330–1341 (2020).

[35] Venter, C. *et al.* Erythrocyte, platelet, serum ferritin, and P-selectin pathophysiology implicated in severe hypercoagulation and vascular complications in COVID-19. *International Journal of Molecular Sciences* **21**, 8234 (2020).

[36] Buonsenso, D. *et al.* Circulating activated platelets in children with Long COVID: a case-controlled preliminary observation. *The Pediatric Infectious Disease Journal* **43**, e430–e433 (2024).

[37] Turner, S. *et al.* Long COVID: pathophysiological factors and abnormalities of coagulation. *Trends in Endocrinology & Metabolism* **34**, 321–344 (2023).

[38] Zhu, A. *et al.* Infection of lung megakaryocytes and platelets by SARS-CoV-2 anticipate fatal COVID-19. *Cellular and Molecular Life Sciences* **79**, 365 (2022).

[39] Pretorius, E. *et al.* Persistent clotting protein pathology in Long COVID/Post-Acute Sequelae of COVID-19 (PASC) is accompanied by increased levels of antiplasmin. *Cardiovascular Diabetology* **20**, 172 (2021).

[40] Pretorius, E. *et al.* Prevalence of symptoms, comorbidities, fibrin amyloid microclots and platelet pathology in individuals with Long COVID/Post-Acute Sequelae of COVID-19 (PASC). *Cardiovascular Diabetology* **21**, 148 (2022).

[41] Kell, D. B., Laubscher, G. J. & Pretorius, E. A central role for amyloid fibrin microclots in Long COVID/PASC: origins and therapeutic implications. *Biochemical Journal* **479**, 537–559 (2022).

[42] Romano, J., Kromrey, J. D., Coraggio, J. & Skowronek, J. Appropriate statistics for ordinal level data: should we really be using t-test and Cohen's d for evaluating group differences on the NSSE and other surveys. Paper presented at the annual

meeting of the Florida Association of Institutional Research (2006).

[43] Venter, C., Pretorius, J. H., Kell, D. B. & Pretorius, E. A novel MetaCyte Metafer classifier for platelet morphology using Long COVID as a model. *Journal of Thrombosis and Thrombolysis* **59**, 664–675 (2026).

[44] Button, K. S. *et al.* Power failure: why small sample size undermines the reliability of neuroscience. *Nature Reviews Neuroscience* **14**, 365–376 (2013).

[45] Soriano, J. B. *et al.* A clinical case definition of post-COVID-19 condition by a Delphi consensus. *The Lancet Infectious Diseases* **22**, e102–e107 (2022).

[46] Kirillov, A., He, K., Girshick, R., Rother, C. & Dollár, P. Panoptic segmentation. *Proceedings of the IEEE/CVF Conference on Computer Vision and Pattern Recognition* 9404–9413 (2019).

[47] Stringer, C. & Pachitariu, M. Cellpose3: one-click image restoration for improved cellular segmentation. *Nature Methods* **22**, 592–599 (2025).

[48] Stringer, C., Wang, T., Michaelos, M. & Pachitariu, M. Cellpose: a generalist algorithm for cellular segmentation. *Nature Methods* **18**, 100–106 (2021).

[49] Pachitariu, M. & Stringer, C. Cellpose 2.0: how to train your own model. *Nature Methods* **19**, 1634–1641 (2022).

[50] Ronneberger, O., Fischer, P. & Brox, T. U-Net: convolutional networks for biomedical image segmentation. *Medical Image Computing and Computer-Assisted Intervention – MICCAI 2015* **9351**, 234–241 (2015).

[51] Lin, T.-Y. *et al.* Microsoft COCO: common objects in context. *Computer Vision – ECCV 2014* **8693**, 740–755 (2014).

[52] Yen, J.-C., Chang, F.-J. & Chang, S. A new criterion for automatic multilevel thresholding. *IEEE Transactions on Image Processing* **4**, 370–378 (1995).

[53] Vincent, L. & Soille, P. Watersheds in digital spaces: an efficient algorithm based on immersion simulations. *IEEE Transactions on Pattern Analysis and Machine Intelligence* **13**, 583–598 (1991).

[54] Paszke, A. *et al.* PyTorch: An imperative style, high-performance deep learning library. *Advances in Neural Information Processing Systems* **32**, 8024–8035 (2019).

[55] Van der Walt, S. *et al.* scikit-image: image processing in Python. *PeerJ* **2**, e453 (2014).

[56] Thon, J. N. & Italiano, J. E. Platelets: production, morphology and ultrastructure. *Handbook of Experimental Pharmacology* **210**, 3–22 (2012).

[57] Diez-Silva, M., Dao, M., Han, J., Lim, C.-T. & Suresh, S. Shape and biomechanical characteristics of human red blood cells in health and disease. *MRS Bulletin* **35**, 382–388 (2010).

[58] Cohen, J. A coefficient of agreement for nominal scales. *Educational and Psychological Measurement* **20**, 37–46 (1960).

[59] Fleiss, J. L. Measuring nominal scale agreement among many raters. *Psychological Bulletin* **76**, 378–382 (1971).

[60] Mann, H. B. & Whitney, D. R. On a test of whether one of two random variables is stochastically larger than the other. *The Annals of Mathematical Statistics* **18**, 50–60 (1947).

[61] Lazic, S. E. The problem of pseudoreplication in neuroscientific studies: is it affecting your analysis? *BMC Neuroscience* **11**, 5 (2010).

[62] Benjamini, Y. & Hochberg, Y. Controlling the false discovery rate: a practical and powerful approach to multiple testing. *Journal of the Royal Statistical Society: Series B (Methodological)* **57**, 289–300 (1995).

[63] Cliff, N. Dominance statistics: Ordinal analyses to answer ordinal questions. *Psychological Bulletin* **114**, 494–509 (1993).

[64] Virtanen, P. *et al.* SciPy 1.0: fundamental algorithms for scientific computing in Python. *Nature Methods* **17**, 261–272 (2020).

Supplementary Files

This is a list of supplementary files associated with this preprint. Click to download.

- supplementary.pdf